Quantifying the response of the ORAC aerosol optical depth retrieval for MSG SEVIRI to aerosol model assumptions

Quantifying the response of the ORAC aerosol optical depth retrieval for MSG SEVIRI to aerosol model assumptions

Claire E. Bulgin,[1] Paul I. Palmer,[1] Christopher J. Merchant,[1] Richard Siddans,[2] Siegfried Gonzi,[1] Caroline A. Poulsen,[2] Gareth E. Thomas,[3] Andrew M. Sayer,[2,3] Elisa Carboni,[3] Roy G. Grainger,[3] Eleanor J. Highwood,[4] and Claire L. Ryder[5]

Received 11 May 2010; revised 21 October 2010; accepted 7 December 2010; published 15 March 2011.

[1] We test the response of the Oxford-RAL Aerosol and Cloud (ORAC) retrieval algorithm for Meteosat Second Generation Spinning Enhanced Visible and InfraRed Imager (MSG SEVIRI) to changes in the aerosol properties used in the dust aerosol model, using data from the Dust Outflow and Deposition to the Ocean (DODO) flight campaign in August 2006. We find that using the observed DODO free tropospheric aerosol size distribution and refractive index increases simulated top of the atmosphere radiance at 0.55 μm assuming a fixed aerosol optical depth of 0.5 by 10–15%, reaching a maximum difference at low solar zenith angles. We test the sensitivity of the retrieval to the vertical distribution of the aerosol and find that this is unimportant in determining simulated radiance at 0.55 μm. We also test the ability of the ORAC retrieval when used to produce the GlobAerosol data set to correctly identify continental aerosol outflow from the African continent, and we find that it poorly constrains aerosol speciation. We develop spatially and temporally resolved prior distributions of aerosols to inform the retrieval which incorporates five aerosol models: desert dust, maritime, biomass burning, urban, and continental. We use a Saharan Dust Index and the GEOS-Chem chemistry transport model to describe dust and biomass burning aerosol outflow and compare AOD using our speciation against the GlobAerosol retrieval during January and July 2006. We find AOD discrepancies of 0.2–1 over regions of intense biomass burning outflow, where AOD from our aerosol speciation and GlobAerosol speciation can differ by as much as 50–70%.

Citation: Bulgin, C. E., et al. (2011), Quantifying the response of the ORAC aerosol optical depth retrieval for MSG SEVIRI to aerosol model assumptions, *J. Geophys. Res.*, *116*, D05208, doi:10.1029/2010JD014483.

1. Introduction

[2] The magnitude and distribution of radiative forcing from aerosols represents one of the largest uncertainties in understanding Earth's climate [*Intergovernmental Panel on Climate Change* (*IPCC*), 2007]. Aerosols affect climate directly by scattering and absorbing solar radiation, and indirectly by modifying cloud microphysical properties. They have a diverse range of natural and anthropogenic sources including desert dust, sea salt, and incomplete fuel combustion leading to different optical properties for each aerosol type. The atmospheric lifetime of these aerosols, determined by size (gravitational settling and uplift size distribution), hygroscopicity (rainout and washout), chemical reactivity (heterogenous chemistry), and meteorology, is of the order of several days. The resulting large spatial and temporal variations in the loading and chemical composition of aerosols are sampled only sparsely by surface and aircraft measurements but are of significant climatic importance. We focus here on aerosol observed by the Spinning Enhanced Visible and InfraRed Imager (SEVIRI), dominated by dust and biomass burning outflow from the African continent. These aerosols have direct and indirect effects on climate, altering the radiative balance and cloud properties which can lead to a reduction in precipitation and sea surface temperature [*Huang et al.*, 2009; *Foltz and McPhaden*, 2008]. Dust deposited over the ocean can also stimulate phytoplankton production [*Mills et al.*, 2004]. Satellite observations provide global measurements of aerosol optical properties (e.g., aerosol optical depth) which are invaluable for improving global quantitative understanding of aerosols and their climate impacts. However, current instruments do not provide enough information to fully constrain aerosol properties eg. size and absorption capability and thus aerosol retrievals rely heavily on a priori assumptions [*Kokhanovsky et al.*, 2010].

[3] Aerosol optical properties are retrieved from satellites by fitting simulated radiances to observed radiances. Simulated radiances are determined using a radiative transfer

[1]School of GeoSciences, Edinburgh University, Edinburgh, UK.
[2]Rutherford Appleton Laboratory, Didcot, UK.
[3]Atmospheric, Oceanic and Planetary Physics, Clarendon Laboratory, Oxford, UK.
[4]Department of Meteorology, University of Reading, Reading, UK.
[5]Department of Physics, Imperial College, London, UK.

0148-0227/11/2010JD014483

model that makes prior assumptions about the surface and atmospheric state (e.g., surface reflectance, aerosol types and associated size distributions). We examine aerosol optical depths (AODs) retrieved from SEVIRI aboard the geostationary Meteosat Second Generation-2 (MSG-2) satellite centered over Africa. We retrieve AOD using the Oxford-Ral Aerosol and Cloud (ORAC) optimal estimation scheme (described in section 2), and use these data to understand continental outflow of aerosols over the Atlantic. In recognition of the fact that the assumed aerosol type will affect the retrieved AOD, the ORAC scheme performs retrievals for each scene for a range of different aerosol types. To assign a "best type" a number of type-specific quality control measures are applied including the quality of fit to the observed radiance (i.e., the cost function). However it was recognized that the skill of this method in distinguishing aerosol type (especially those with similar optical properties) would be limited. Here, we develop a temporally and spatially resolved speciation to inform the ORAC retrieval.

[4] The results we present are split into two complementary sections: (1) in section 3 we use detailed aircraft observations to evaluate the aerosol size distribution shape, refractive index, and aerosol vertical distribution assumed by ORAC in Saharan dust outflow over the Atlantic and quantify the impact of these assumptions and solar geometry on the simulated radiance and resulting AOD retrievals; and (2) in section 4 we develop a new seasonal aerosol speciation using the brightness temperatures from SEVIRI to provide information about dust, and output from a chemistry transport model to provide information on the transport of biomass burning aerosol outflow. We quantify the impact of these new speciation distributions on retrieved AOD in section 5 and conclude the paper in section 6.

2. SEVIRI Instrument and Algorithm Description

2.1. SEVIRI

[5] SEVIRI aboard the MSG-2 satellite was launched at the end of 2005 in an equatorial geostationary orbit centered over Africa and makes observations every 15 min. SEVIRI measures reflected solar and infrared radiation in eleven spectral channels centered near 0.6, 0.8, 1.6, 3.9, 6.2, 7.3, 8.7, 9.7, 10.8, 12, and 13.4 μm, with a spatial resolution of 3×3 km in the nadir which gets coarser with distance from the nadir [*Schmetz et al.*, 2002]. SEVIRI also has a broadband high-resolution visible channel covering the 0.6 and 0.8 μm spectral bands giving data with a spatial resolution of 1×1 km in the nadir.

2.2. The ORAC Retrieval Scheme

[6] ORAC retrieves AOD, aerosol effective radius and surface albedo using the 0.6, 0.8 and 1.6 μm SEVIRI radiances. It uses an optimal estimation approach, varying all retrieved parameters simultaneously (aerosol optical depth, aerosol effective radius and surface reflectance), to calculate the retrieved state with the maximum probability, whilst accounting for both measurements and a priori data and uncertainties in both [*Rodgers*, 2000]. It uses the DIScrete Ordinances Radiative Transfer model (DISORT) [*Stammes et al.*, 1988] to calculate top of the atmosphere (TOA) radiance as a function of the properties of a plane parallel aerosol or cloud layer with an assumed height distribution. The retrieval scheme was originally developed for clouds [*Watts et al.*, 1998] and applied to data from the Along Track Scanning Radiometer (ATSR), and later extended to aerosol retrievals from ATSR [*Marsh et al.*, 2004] and other instruments. A full description of the ORAC retrieval scheme is provided by *Thomas et al.* [2009a].

[7] The ORAC forward model, $\mathbf{F}$, consists of four separate elements: (1) a model of aerosol scattering and absorption; (2) a model of atmospheric gas absorption; (3) a model of atmospheric radiative transfer; and (4) a model of surface reflectance [*Thomas et al.*, 2007], which uses aerosol optical properties calculated offline to interpret the observed radiances. The optical properties used in the aerosol model (aerosol phase function, extinction and scattering coefficients) are calculated using Mie theory from prior information about aerosol size distributions and refractive indices from observations and modeling studies [*Hess et al.*, 1998; *Dubovik et al.*, 2002]. These properties are calculated as a function of aerosol effective radius, ranging between 0.01 and 10 μm, by varying the mixing ratio of the different components within each aerosol type. These are collected together within the model in a series of look-up tables (LUTs) describing atmospheric transmission and reflectance, for radiance and AOD calculations.

[8] The forward model is fitted to the observed radiances by minimizing a cost function $J(\mathbf{x})$ which describes the quality of fit between the observed radiances (the measurement vector $\mathbf{y}$) and modeled radiances, the state vector $\mathbf{x}$ and the a priori state vector $\mathbf{x}_a$,

$$J(\mathbf{x}) = (\mathbf{F}(\mathbf{x}) - \mathbf{y})\mathbf{S}_y^{-1}(\mathbf{F}(\mathbf{x}) - \mathbf{y})^{\mathrm{T}} + (\mathbf{x} - \mathbf{x}_a)\mathbf{S}_a^{-1}(\mathbf{x} - \mathbf{x}_a)^{\mathrm{T}}, \quad (1)$$

where $\mathbf{S}_y$ and $\mathbf{S}_a$ are the error covariance matrices for the measurement vector and the a priori state vector, respectively. A priori and measurement errors are assumed to be normally distributed with zero mean, and variance determined by measurement and forward model noise ($\mathbf{S}_y$) and a priori error ($\mathbf{S}_a$) [*Thomas et al.*, 2007]. ORAC uses the Levenberg-Marquardt algorithm to minimize the cost function and subsequently identify the state vector that is most consistent with $\mathbf{x}_a$, $\mathbf{y}$, $\mathbf{S}_y$, and $\mathbf{S}_a$ [*Thomas et al.*, 2009a]. The problem is moderately nonlinear with the number of required iterations generally below the upper limit of 25, a number indicative of a failed retrieval [*Thomas et al.*, 2009b].

[9] We limit our analysis of AOD to ocean scenes where low surface albedo at wavelengths of interest make it easier to separate surface reflectance from the aerosol signal in the retrieval and we use a fixed spectral shape to describe ocean reflectance [*Thomas et al.*, 2005]. Cloudy scenes are removed prior to fitting using the EUMETSAT cloud mask derived using reflectance, temperature, snow and ice tests at the full SEVIRI spatial resolution [*Thomas et al.*, 2005], and a spatial coherence test is used to remove spatially isolated high AOD under the assumption that this is cloud.

[10] The ORAC scheme uses five aerosol models: continental, urban, maritime, desert dust and biomass burning. Each model is constructed from a number of lognormally distributed aerosol components with different modal radii and spread. The mixing ratios of each component of the aerosol a priori are varied to allow aerosol effective radius to range between 0.01 and 10 μm in the retrieval. Desert dust, maritime, urban and continental aerosol are defined using

refractive index and component size distribution data from the Optical Properties of Aerosols and Clouds (OPAC) package [*Hess et al.*, 1998]. For biomass burning aerosol, these properties are defined from three years of in situ data from the AErosol RObotic NETwork (AERONET) [*Dubovik et al.*, 2002].

[11] The retrieval assumes spherical particles for all aerosol classes and aerosol optical properties are derived using Mie theory. Previous research has shown that this assumption is unlikely to be correct for dust particles eg. [*Otto et al.*, 2009; *Zhao et al.*, 2003], although dust particle shape is at present poorly constrained and the information content of current retrievals is often insufficient to distinguish between spherical and nonspherical particles [*Wang et al.*, 2003]. The assumption of spherical dust particles was used in the GlobAerosol product (section 2.3) and provides consistency with the derivation of aerosol optical properties from DODO measurements. It is also used in most other well-known aerosol retrieval schemes for instruments such as the Moderate Resolution Imaging Spectroradiometer (MODIS) [*Remer et al.*, 2006], with the exception of the Multiangle Imaging SpectroRadiometer (MISR) which has the ability to resolve scattering at multiple angles [*Diner et al.*, 2008].

2.3. GlobAerosol Data Product

[12] GlobAerosol was a project to develop a merged global AOD data set between 1995 and 2007 using instruments on a number of European satellite platforms; ATSR-2, the Advanced Along Track Scanning Radiometer (AATSR), the Medium Resolution Imaging Spectrometer (MERIS) and SEVIRI. The SEVIRI AOD is derived using the ORAC retrieval algorithm on a 10 × 10 km sinusoidal grid. GlobAerosol uses the retrieved aerosol optical properties for each of the five aerosol models included in the ORAC retrieval because there is not sufficient information in the retrieval to unambiguously identify aerosol type. The "best" retrieved aerosol type is determined by the smallest retrieval cost following quality control, as defined above. Costs for different aerosol classes can be similar thereby compromising this approach.

[13] In section 3 we test the sensitivity of the retrieval to the defined aerosol a priori, a requirement for evaluating the robustness of long-term data sets used to define aerosol radiative forcing. Other well-known retrieval schemes for instruments including MODIS and MISR take a similar approach to ORAC using predefined aerosol models and prior climatological probabilities [*Diner et al.*, 1999, 2008] or a mixture of coarse and fine mode particles [*Remer et al.*, 2006] to model retrieved radiance. Our work therefore has a wider application beyond the ORAC scheme to many satellite retrieval schemes.

3. Sensitivity of ORAC Scheme to the a Priori Optical Properties, Vertical Distribution of Aerosols, and the Viewing Geometry

[14] The purpose of this section is to test the robustness of the assumptions about dust aerosol used in the ORAC scheme, including size distribution, refractive index, phase function and vertical distribution; and how sensitive the simulated radiance is to changing these assumptions. Previous studies have highlighted the importance of particle size distribution and refractive index to simulated top of the atmosphere (TOA) radiance and retrieved aerosol optical depth [*Liao and Seinfeld*, 1998; *Durant et al.*, 2009; *Martonchick et al.*, 2002]. Retrieval sensitivity to these parameters is dependent on the aerosol model assumption used and needs to be evaluated independently for any algorithm from which aerosol forcing is to be calculated. We achieve this for the ORAC scheme using relatively sparse but detailed data from the Dust Outflow and Deposition to the Ocean (DODO) aircraft campaign described below. We also assess the sensitivity of the retrieved AOD to the viewing geometry, and compare the DODO AOD and aerosol effective radius with data from the retrieval.

3.1. Description of the DODO Aircraft Campaign Data

[15] The DODO aircraft campaign took place over Western Africa and the Eastern tropical Atlantic during February and August 2006 with the aim of quantifying iron deposition to the ocean, and was affiliated with the African Monsoon Multidisciplinary Analysis (AMMA) project [*McConnell et al.*, 2008; *Rajot et al.*, 2008]. We use data collected during August 2006 when the FAAM BAe146 aircraft was based in Dakar, Senegal, making in situ and remote airborne measurements of dust aerosol. Aerosol size distribution was measured using the Passive Cavity Aerosol Spectrometer Probe (PCASP) and the Cloud Droplet Probe (CDP) and we refer the reader elsewhere for a more detailed description of the data collection [*McConnell et al.*, 2008].

[16] We use DODO aircraft measurements of aerosol properties averaged across horizontal flight paths (referred to as "runs" abbreviated to "R") covering between 30 and 200 km, or as vertical profile data (abbreviated to "P") extending from ~50 m to a maximum altitude of 6 km, above which aerosol concentrations were negligible. Data from the PCASP and CDP instruments together provide aerosol size distributions at 0.55 μm over the 0.05–20 μm radius size interval in both the horizontal runs and vertical profiles. We also use refractive indices from DODO, inferred from Mie scattering calculations, which are only available at 0.55 μm [*McConnell et al.*, 2008, 2010]. We use the size distributions and refractive indices in offline Mie scattering calculations to generate aerosol optical properties including aerosol effective radii, phase function and extinction coefficients from both the horizontal run and vertical profile data.

[17] For this paper, we use data from three flying days during the DODO campaign and focus first on the horizontal run data. Flights are labeled with a prefix "b" and a flight number. We use data from flight b237 (22 August 2006) runs R1, R3, R4, R5, R6, R7; flight b239 (24 August 2006) runs R1, R2-4, R5, R6; and flight b241 (25 August, 2006) R2. All flights sampled free tropospheric aerosol between 800 and 500 hPa, with the exception of flight b237 runs R4 and R5, which sampled boundary layer aerosol at approximately 1000 hPa. From this point on we will distinguish between the free troposphere (FT) and the boundary layer (BL) data. Further details of the flight tracks are given by *McConnell et al.* [2008].

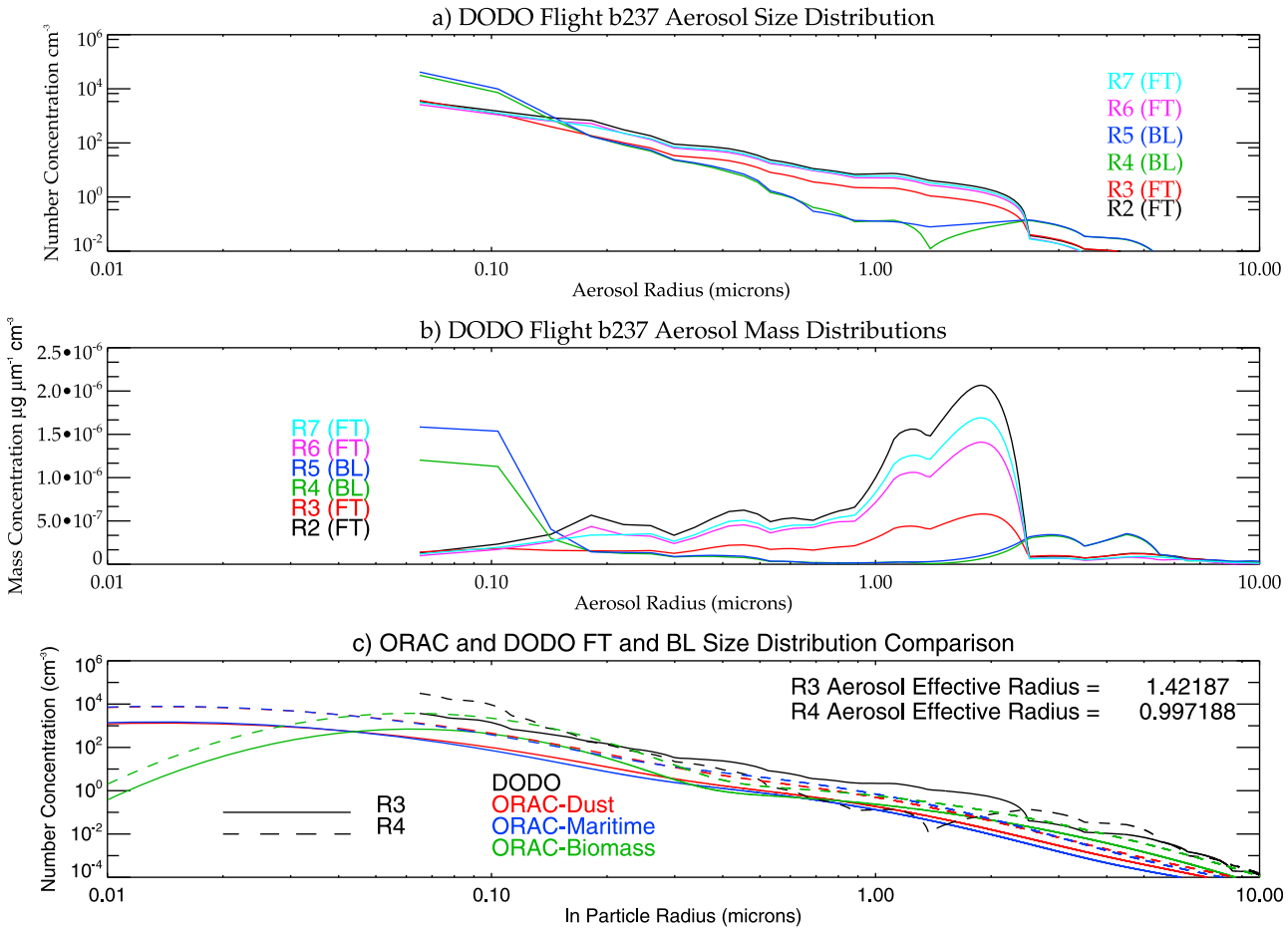

Figure 1. Observed (a) aerosol number (cm^{-3}) and (b) mass distributions (μg μm^{-1} cm^{-3}) as a function of aerosol radius (μm) for DODO flight b237, 22 August 2006, and (c) observed aerosol size distributions for typical boundary layer and free troposphere conditions during DODO, with the corresponding OPAC model values for dust (red), maritime (blue), and biomass burning (green) aerosol. OPAC aerosol model data are matched to the DODO data using the DODO aerosol effective radii and number distribution.

3.2. Aerosol Size and Mass Distribution

[18] Figure 1a shows observed FT and BL aerosol size distributions, and Figure 1b shows mass distributions calculated assuming a dust density of 2.65 g cm^{-3} [*Tegen and Fung*, 1995], on 22 August 2006 during DODO. The aerosol modal radii in the FT is <0.1 μm, above which number concentration decreases with increasing aerosol radius. BL number concentrations of fine mode aerosol (<0.1 μm radius) are 5 times larger than those in free tropospheric air; there are also more large particles (2.5–4 μm radius) present in the BL although total aerosol number concentrations are greater in the FT. Figure 1b shows that BL aerosol mass distribution peaks below 0.2 μm radius and between 2 and 5.5 μm radius; in contrast, most of the FT aerosol mass is between 0.2 and 2 μm radius. Coarse mode aerosol (>1 μm radius) is lost from the FT due to gravitational settling. Observed variations in aerosol distribution may also reflect different source regions. Ten day back trajectories from the location of the DODO flights using the NOAA HYSPLIT model (R. R. Draxler and G. D. Rolph, HYSPLIT (HYbrid Single-Particle Lagrangian Integrated Trajectory) model, 2010, http://ready.arl.noaa.gov/HYSPLIT.php) (not shown), and 5 day back trajectories using the NAME model [*McConnell et al.*, 2010] indicate that sampled air masses over the Atlantic have a range of potential geographical sources including Libya, Algeria, Mauritania and the western Sahara.

[19] Figure 1c compares typical observed DODO and ORAC aerosol model size distributions in the FT and BL matched on the basis of the DODO aerosol number concentration and effective radius. Effective radius is not fixed in the retrieval; however the lognormal distribution $n(r)$ for each of the components in the assumed aerosol model is defined as

$$n(r) = \frac{N_0}{\sqrt{2\pi}} \frac{1}{ln(s)} \frac{1}{r} \exp\left[-\frac{(ln(r) - ln(r_m))^2}{2ln^2(s)} \right], \qquad (2)$$

where N_0 is the total number concentration, r_m the median radius of the aerosol, and s is the spread of the distribution. We find that the observed DODO number distributions at radii >0.05 μm, based on data from a FT and a BL flight, are greater than the ORAC aerosol models. The ORAC dust and maritime aerosol size distributions are similar, whilst the biomass burning aerosol is characterized by fewer fine mode

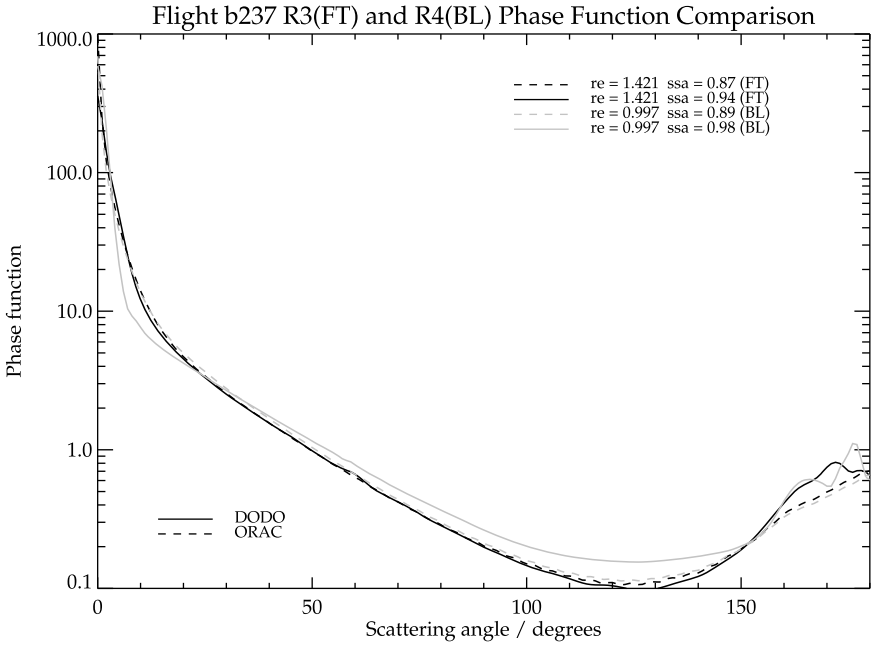

Figure 2. Phase functions at 0.55 μm derived from DODO observations (solid line) and ORAC dust model (dashed line) phase functions on 22 August 2006, which is representative of the conditions found for the boundary layer and the free troposphere during the DODO aircraft campaign. The model correspondence to the data is determined by the observed aerosol effective radii. The single scattering albedo is given for the DODO and ORAC data.

particles (<0.045 μm) and higher number concentrations between 0.045 and 0.3 μm radius. We acknowledge that the lower detection limit of 0.05 μm radius in the DODO data may bias these comparisons as they are based on the total aerosol number concentration.

3.3. Scattering Phase Functions

[20] Figure 2 compares aerosol phase functions calculated using the DODO size distributions and refractive index, and the ORAC dust model, matched using the DODO aerosol effective radius. They have been compared for aerosol effective radii from two flights indicative of FT and BL data at 0.55 μm. We accept that FT and BL aerosol properties cannot be distinguished between in the retrieval and only column values can be determined, but separating these data here gives a range of observed size distributions to test retrieval sensitivity. In the FT, ORAC and DODO phase functions are almost identical except at near-backscattering angles (160°–180°) where DODO data shows a double peak in scattered light intensity with a maximum difference in magnitude of 0.3. The additional observed peaks in the phase function may reflect the noisier distribution of aerosol particles with radii <0.1 μm than described by the ORAC distribution. DODO backscattered radiation intensity may also be limited by the lower observation limit of 0.05 μm radius. In the BL, a similar feature is seen a near-backscattering angles. DODO data also shows greater scattering between 50° and 100° with an absolute difference of 0.1, and a sharper forward scattering peak observed between 0° and 8° compared with 0°–15° for the DODO data. We also find that the DODO observations have a significantly higher single scattering albedo (0.94–0.98) than the ORAC model (0.87–0.89) which is taken from OPAC [*Hess et al.*, 1998]. We recalculate the phase function using the DODO size distribution and the ORAC complex refractive index (not shown). For both distributions the real part of the refractive index is the same with a value of 1.53. We find that the discrepancy in the single scattering albedo can be attributed to the much lower DODO imaginary refractive index (0.0018(R3), 0.0003(R4)) compared to 0.0055 in the ORAC model. In the retrieval the dust aerosol is assumed to be more absorbing than the dust sampled during DODO and other aircraft campaigns [*McConnell et al.*, 2008; *Osborne et al.*, 2007].

3.4. Viewing Geometry

[21] Observed aerosol radiances are influenced by the Sun instrument geometry because the aerosol phase function is dependent on the angle of observation. Here we use the ORAC forward model (section 2.2) to test the sensitivity of the simulated radiance to scattering angle as a function of solar zenith angle (SZA). Figures 3 and 4 show TOA model radiances simulated using DODO observations and the ORAC dust aerosol model between 0800 and 1745 local time (LT). We match the ORAC aerosol effective radius to the observed DODO effective radius and assume a fixed aerosol optical depth of 0.5. We compare the difference in simulated TOA radiance between the ORAC and DODO models using the DODO size distribution and DODO refractive index (Figure 3), and the DODO size distribution with the ORAC refractive index (Figure 4). Radiances are calculated in a pseudo 0.55 μm channel, generated to match DODO observations with the ORAC model, as SEVIRI does not make observations at this wavelength. Profiles of atmospheric temperature, water vapor and ozone for each retrieval are taken from the European Centre for Medium-

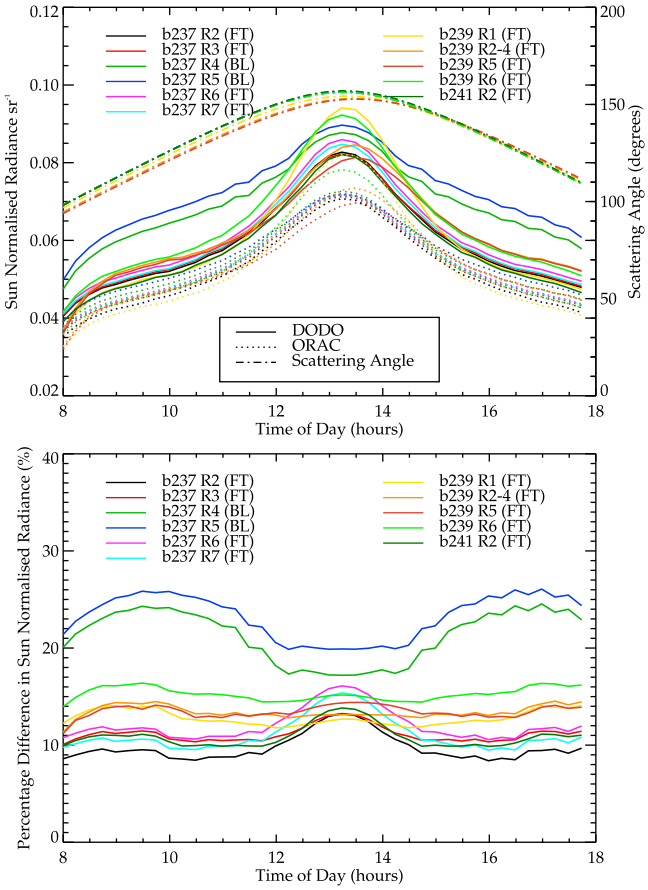

Figure 3. (top) Forward model Sun normalized radiances (sr^{-1}) corresponding to DODO (solid line) and ORAC dust (dashed line) a priori, matched by aerosol effective radius and using DODO and ORAC refractive indices described as a function of time of day, and (bottom) their percentage difference. Radiances are shown for different flights and for the free troposphere (FT) and the boundary layer (BL). All calculations assume an aerosol optical depth of 0.5.

range Weather Forecasting (ECMWF). In both cases, simulated radiances peak between 1200 and 1400 LT at a scattering angle of ~150°, which is as expected given that the phase function intensity peaks at near-backward scattering angles.

[22] Figure 3 shows that radiances simulated using the DODO size distribution and refractive index are generally larger than those derived using the ORAC dust model. In the FT, the DODO observations are ~10% higher than the ORAC values before midday and after 1400, increasing to ~15% between those times. In the BL, the bias is ~25% during the morning and afternoon, decreasing to ~20% when the Sun is overhead. FT phase function differences between DODO and ORAC are most pronounced at near-backscattering angles. BL data shows greater scattering by DODO aerosol between 100° and 150° as well as between 160° and 180° explaining the larger DODO radiances throughout the day. We find that this difference in retrieved radiance is sensitive to changes in AOD, increasing by ~2–4% between an optical depth of 0.4 and 0.6. We acknowledge that Mie code assuming spherical particles may not define the dust phase function correctly and suggest that variance in modeled radiance with SZA using this regime should not be overinterpreted.

[23] From the comparison using the ORAC refractive index with the DODO size distribution (Figure 4) we find that the systematic high bias in the DODO simulated radiance can be attributed to the lower imaginary refractive index. When we use the ORAC refractive index we find that TOA radiance is similar for both size distributions in the FT data. Differences are less marked at high scattering angles as we find that combining the ORAC refractive index with the DODO size distribution data lowers the phase function at near-backscattering angles to values comparable with the ORAC dust model (not shown). In the BL, the DODO aerosol retains its larger scattering feature between 100° and 150° and flatter diurnal response to changes in SZA.

[24] We assess the sensitivity of the simulated radiances in the retrieval to changes in the assumed vertical distribution of aerosol by comparing the ORAC extinction coefficient profile shape and the observed DODO extinction coefficient profile. The ORAC dust profiles assume that most of the

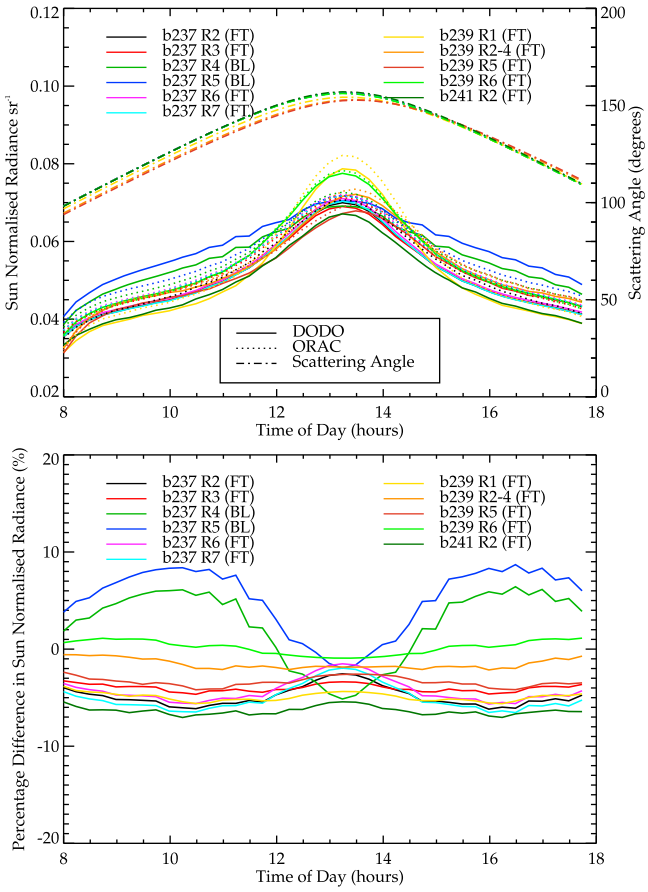

Figure 4. (top) Forward model Sun normalized radiances (sr^{-1}) corresponding to DODO (solid line) and ORAC dust (dashed line) a priori, matched by aerosol effective radius and using only ORAC refractive indices described as a function of time of day, and (bottom) their percentage difference. Radiances are shown for different flights and for the free troposphere (FT) and the boundary layer (BL). All calculations assume an aerosol optical depth of 0.5.

dust aerosol is concentrated below 2 km altitude with a linear decrease in aerosol burden between 2 and 3 km. In dusty regions in summer months this is a poor assumption as dust laden air from the BL is frequently lofted to 4–6 km [*Z. Liu et al.*, 2008; *D. Liu et al.*, 2008]. When we test the forward model using both vertical profiles we find a difference of <1% in simulated radiance at 0.55 μm. At other wavelengths the vertical distribution of aerosol may be more important, particularly in the 0.8 μm channel where absorption by water vapor in the BL may enhance or dampen the aerosol signal depending on the relative location of the aerosol.

4. Development of Seasonal Information to Constrain Aerosol Type

[25] We described previously the approach taken in the ORAC retrieval for the GlobAerosol data set to determine aerosol speciation (section 2.3). Without making assumptions about aerosol a priori it is not possible to infer aerosol optical properties from current satellite retrievals. The work we showed in section 3 clearly indicates that accurate details of aerosol type and optical properties are critical to making an informed interpretation of aerosol properties from measured radiance. Here we test the ability of the ORAC retrieval to accurately classify aerosol type by choosing the correct aerosol model given no prior information about aerosol spatial distribution, i.e., using the retrieval cost function to decide after applying quality control criteria to each aerosol type. We use a Saharan Dust Index (SDI) and the GEOS-Chem chemistry transport model as tools to describe distributions of dust and biomass burning aerosol and assess the response of the retrieved AOD to the assumed aerosol speciation. The three major aerosol types observed across the SEVIRI field of view are marine aerosol over the ocean, and dust and biomass burning emissions both over the African continent and advected across the Atlantic. We examine dust and biomass burning aerosol in turn below.

4.1. Desert Dust Aerosol

[26] Desert dust aerosol is a mixture of minerals lofted into the atmosphere by the action of wind over arid regions [*Haywood and Boucher*, 2000]. We use a Saharan Dust Index (SDI), originally developed to identify aerosol contamination in nighttime sea surface temperature retrievals [*Merchant et al.*, 2006], to determine dust distributions as a function of season and time of day. The SDI is calculated at the native SEVIRI spatial resolution of 3 × 3 km using data supplied by EUMETSAT (EUropean organisation for the exploitation of METeorological SATellites Unified Meteorological Archive and Retrieval Facility (U-MARF) online ordering, 2009, http://archive.eumetsat.int/umarf/) (hereinafter EUMETSAT Web site, 2009).

[27] The SDI uses variance in 3D brightness temperature difference space to indicate dust in satellite retrievals. Nighttime SDI values are calculated through principal component analysis (PCA) of brightness temperatures in different channels (3.9–8.7 μm, 3.9–12 μm and 11–12 μm), separating the variance caused by changing atmospheric variables such as water vapor identified along PC1, from variance induced by aerosol presence identified by PC2 [*Merchant et al.*, 2006]. During the daytime this algorithm has to be adapted because the 3.9 μm channel is contaminated by solar radiation. We do this by using a local regression between daytime radiance in the three available channels and nighttime SDI values. The regression coefficients for estimating SDI without this channel are found to be valid over a length scale of ~200 km and time scale of ~1 day; beyond which they are decorrelated [*Merchant*, 2006]. To calculate SDI during the day we split the 0000 LT SEVIRI nighttime image into 3364 boxes (~192 × 192 km resolution in the nadir) to generate these local regression constants between observed brightness temperatures in the 8.7, 11 and 12 μm channels and the calculated nighttime SDI for cloud-free pixels. We interpolate this information to the higher-resolution retrieval grid (3 × 3 km in the nadir). We perform the daytime SDI calculation using the local regression constants from the 0000 LT nighttime SDI from the preceding and succeeding days to generate two distributions. The SDI for any intervening hour is calculated from these two distributions and is weighted according to the time of day. The SDI is scaled for convenience to be comparable to observed AOD so that dust is identified when SDI is in the range 0.25–2.0. Further details of the SDI derivation are provided by *Merchant et al.* [2006] and *Merchant* [2006].

[28] We identify cloud-free scenes using the EUMETSAT cloudmask (EUMETSAT Web site, 2009). Optically thin cirrus cloud or cloud edges incorrectly classified as aerosol can result in erroneous SDI values. To reduce the cloud edge error we extend the cloudmask one pixel in each direction. To remove noisy scenes indicative of contamination due to isolated subpixel or incorrectly classified cloud, we discard scenes where the local standard deviation in the SDI over a moving 3 × 3 pixel window, on the 3 × 3 km grid, exceeds 0.2 for nighttime values and 0.1 for daytime values, as aerosol properties are coherent over relatively long spatial scales in clear skies in comparison with clouds. The local regression tends to dampen extreme values reducing data noise, hence the lowered daytime threshold value for discarding noisy scenes.

[29] We calculate the probability of dust aerosol as the fraction of SEVIRI clear-sky scenes where the calculated SDI is between 0.25 and 2.0. For these calculations, we use hourly SDI values between 0800 and 1600 LT every day during 2006, which is limited by measurement availability on only a few days. To reduce contamination from persistent cloud we discard pixels where fewer than 20% of the total scenes are clear. Figure 5 shows the seasonal probability of dust aerosols during the morning (0800–1000), midday (1100–1300), and afternoon (1400–1600). Figure 5 shows that the SDI captures the seasonal variation in dust outflow over the Atlantic, Mediterranean and Red sea, peaking in JJA [*Engelstaedter and Washington*, 2007]. The data shows that dust emissions migrate northward with the Intertropical Convergence Zone from DJF to JJA. We also find persistent dust emissions around the south west African coast likely originating from the Namibian and Kalahari deserts. Our analysis indicates that the flux of dust aerosols across the Atlantic shows no diurnal dependence. High dust probabilities in the polar regions are likely to be an artifact of the high viewing zenith angle.

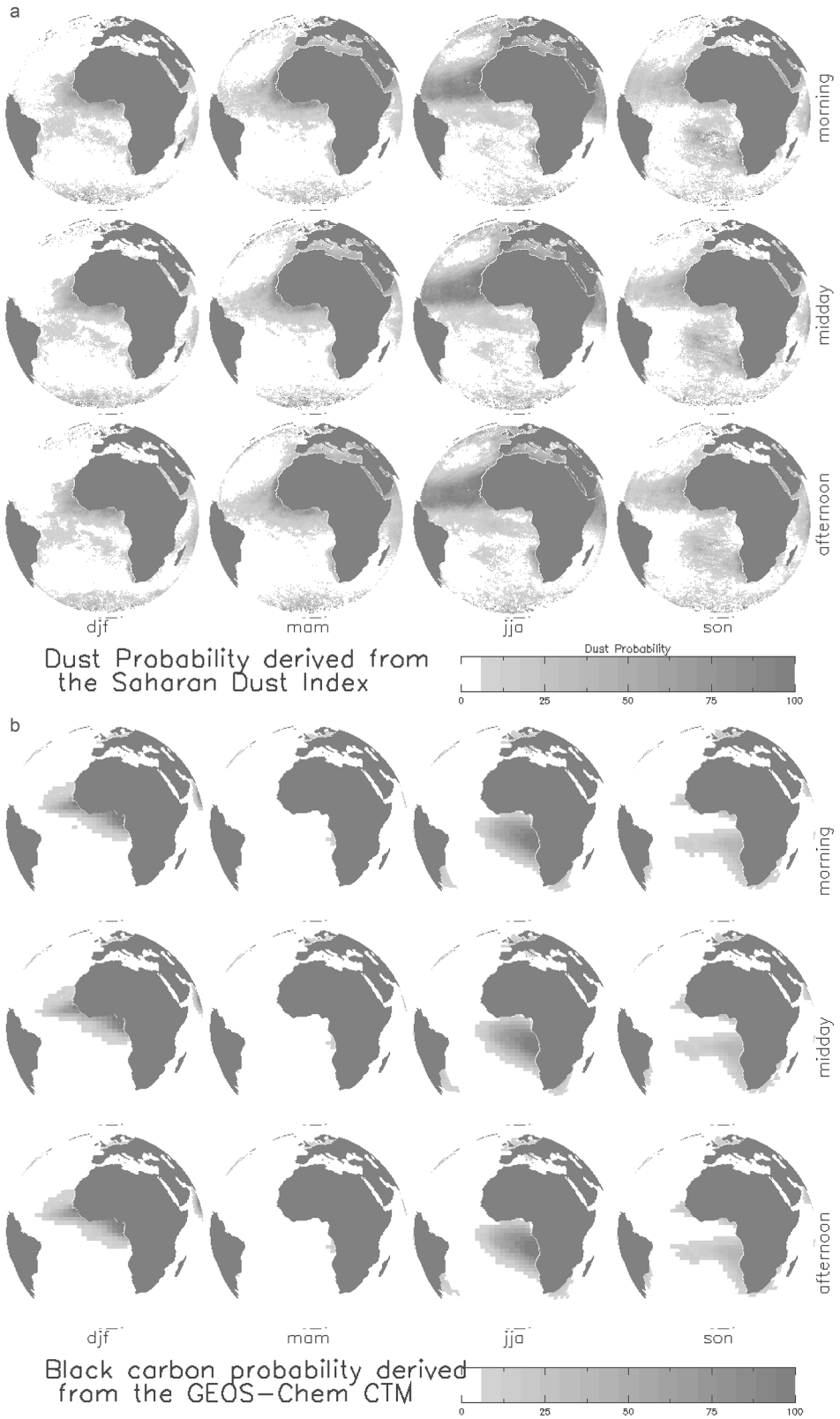

Figure 5. The independent seasonal probability of (a) dust and (b) black carbon, during the morning (0800–1000), midday (1100–1300), and afternoon (1400–1600) for 2006. The probability of dust aerosols was determined by the SDI, and the probability of black carbon determined by the GEOS-Chem chemistry transport model. SDI is calculated at the native SEVIRI resolution of 3 × 3 km in the nadir. GEOS-Chem simulations are at 2 × 2.5° resolution.

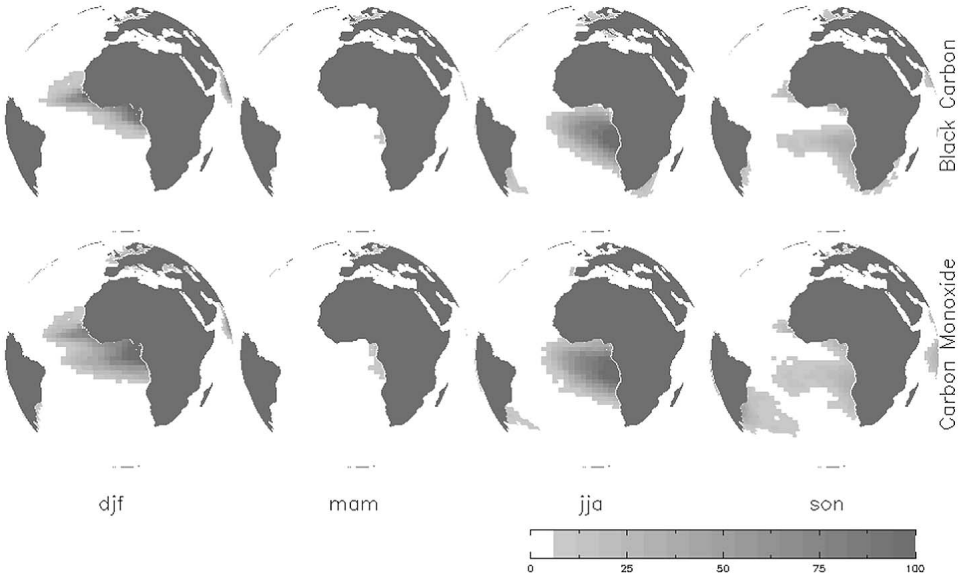

Figure 6. The independent seasonal probability of the presence of CO and black carbon aerosols between 1100 and 1300 LT for 2006. The probability, determined by the GEOS-Chem model, is evaluated on the 2 × 2.5° model grid.

4.2. Biomass Burning Aerosol

[30] Biomass burning generates black carbon (BC), a highly absorbing aerosol via incomplete combustion [e.g., *Haywood and Boucher*, 2000]. We use the BC tracer in the GEOS-Chem chemistry transport model (CTM, described in Appendix A) to identify the distribution of biomass burning aerosol, using model carbon monoxide (CO), another tracer of incomplete combustion, to help evaluate BC transport in the model. CO and BC are emitted primarily through incomplete combustion processes and share many similar sources, including biomass burning, and show similar distributions. First, we evaluate the global model CO using column observations from the NASA Tropospheric Emission Spectrometer (TES). The model captures 45–81% of monthly variation in CO observed by TES, with the exception of JJA, where the correlation is <0.6. We include a more detailed description of GEOS-Chem, TES, and their comparison including evaluation of CO and BC distributions and model performance in Appendix A.

[31] We calculate the probability of BC emissions using a column optical depth threshold of 0.015 to identify BC aerosol within the troposphere, accounting for aerosol transport from the surface layer. We acknowledge that this threshold may seem low for identifying enhanced aerosol loading but is appropriate given the optical depth output from the model. A similar probability measure is used to identify CO emissions where concentrations in an individual layer exceed background levels of 200 ppbv [*Sinha et al.*, 2003]. Figure 6 shows CO and BC fields sampled from the model at midday (1100–1300). There is little variation within each season in the CO and BC distribution with time of day. The distributions of CO and BC are similar, as expected, but there are differences which reflect the different residence times of CO and BC. We find a strong near-source relationship between CO and BC reflecting the commonality of their source. BC is removed from the atmosphere more rapidly than CO which has a lifetime of 1–4 months, removed primarily through oxidation by the OH radical. Figure 5 shows the seasonal probability distributions of BC for morning (0800–1000), midday (1100–1300), and afternoon (1400–1600) calculated from hourly samples corresponding to the SEVIRI SDI. The seasonal distribution describes the southward migration of African fires as the year progresses, consistent with fire count data [*Collatz et al.*, 2007]. Similar calculations were done for organic carbon (not shown), another possible proxy for biomass burning, but we found less agreement with CO than BC due to widespread noncombustion organic carbon sources.

4.3. Combined Aerosol Classification

[32] Figure 7 shows "best type" SEVIRI AOD for 1012, 1312, and 1612 GMT on 22 24, and 25 August 2006, corresponding to flights from the DODO aircraft campaign (described in section 3.1). According to GlobAerosol the "best type" aerosol over the majority of the Atlantic is dust, despite JJA being the peak burning season over southern Africa [*Collatz et al.*, 2007] fueling transport of biomass burning aerosol across the Atlantic.

[33] As shown above the SDI and GEOS-Chem model predict a distinct seasonal variation in the distribution of aerosol over the Atlantic. Figure 7 shows no evidence of the coherent dust or biomass burning plumes expected during JJA in the retrieval, which contains no spatially or temporally resolved prior information about aerosol type and distribution. We suggest here a new approach to selecting aerosol type, using this information from the SDI and GEOS-Chem to inform the ORAC retrieval. We combine the individual probabilities from the desert dust and biomass burning aerosol distributions described above to give a conditional probability given the aerosol is present, of each single aerosol type or combination as a function of location, season and time of day. We use one minus the total probability of all other aerosol classes to determine where "no aerosol" is most likely. In these regions we assume that background

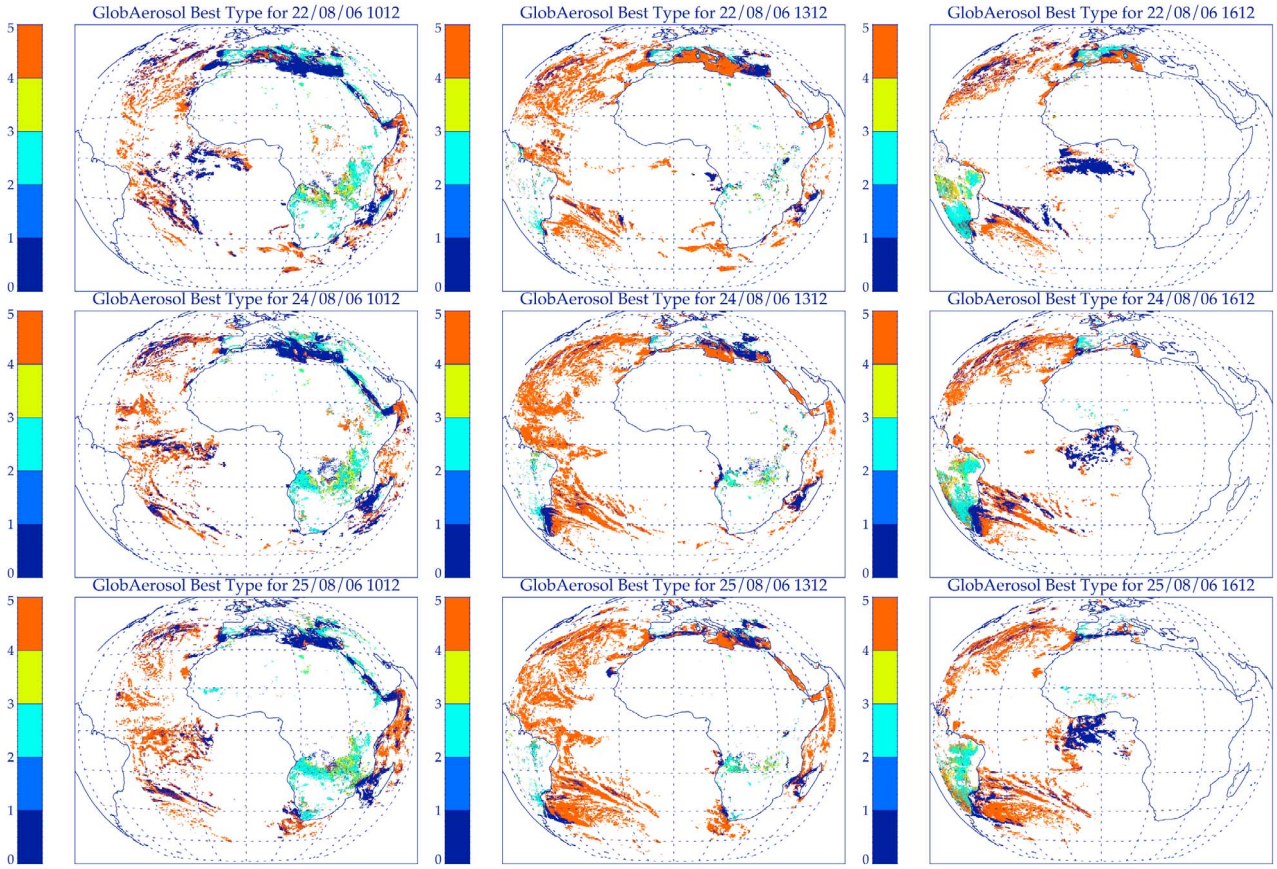

Figure 7. GlobAerosol "best aerosol type" for SEVIRI radiances at 10 × 10 km resolution at 1012, 1312, and 1612 on 22, 24, and 25 August 2006, corresponding to the days of data collection during the DODO campaign. The "best type" is determined from the retrieval cost following quality control for different aerosol types: maritime (1), urban (2), continental (3), biomass burning (4), and desert dust (5).

marine aerosol is present and that the maritime aerosol model should be used in the retrieval.

[34] Figure 8 shows the most likely aerosol class constructed from the probabilities across the SEVIRI disk as a function of season. In DJF we find that the biomass burning aerosol plume over the eastern equatorial Atlantic is commonly collocated with dust. In MAM, dust is the dominant aerosol outflow from the African continent. In JJA dust and biomass burning aerosol outflow form two distinct plumes. In SON aerosol outflow from the African continent is significantly reduced. This information could be used to inform the retrieval and reduce the number of aerosol models processed for each pixel. We suggest that these distributions along with their associated error could be used as a statistical constraint in the ORAC retrieval for a Bayesian inference of aerosol optical properties from observed radiance. In this approach the cost function may be used to help differentiate between aerosol classifications with similar probabilities.

[35] In DJF we find a region where dust and biomass burning aerosol are consistently collocated just off the west African coast. We have no evidence to suggest that these aerosol types are directly mixed and they would likely be found at different altitudes as observed during the Dust and Biomass Experiment (DABEX) campaign [*Johnson et al.*, 2008]. In this instance a two layer model is needed to accurately simulate the radiative transfer of the aerosol present which is not currently available in the SEVIRI ORAC retrieval. We acknowledge that Figure 8 does not indicate how close the probability of the most likely class is to that of other classes and whether the additional information from the cost function would be needed to distinguish between aerosol class, but this is available for inclusion in the retrieval.

5. Retrieval Sensitivity to Constraining Aerosol Type

[36] We test here the sensitivity of the ORAC AOD retrieval to aerosol speciation, comparing selection based on the cost function as implemented in the GlobAerosol retrieval, with aerosol selection based on our speciation maps. As described above, our aerosol classification contains an additional aerosol class, 'dust and biomass burning' which is not currently included in the GlobAerosol retrieval. To make a comparison at present between the two schemes, where dust and biomass burning are collocated in our speciation we assign no aerosol class and no retrieval is made. At 1312, the retrieval time used for this comparison this region often coincides with regions of Sun glint where no aerosol

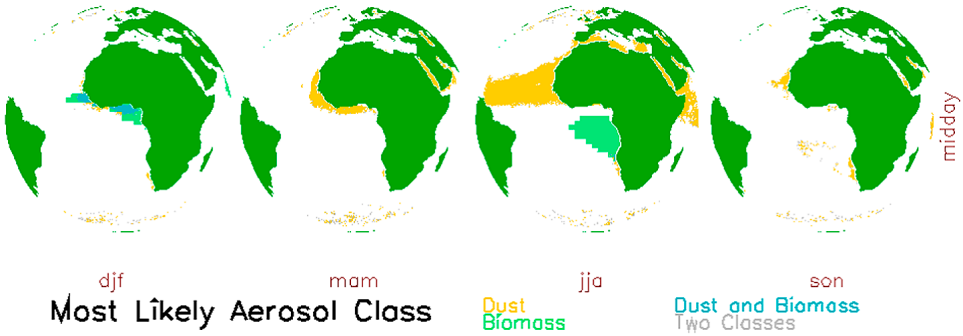

Figure 8. Aerosol type or combination with the highest probability as a function of season for 2006. White areas indicate background marine aerosol. Two classes refers to instances where two individual aerosol classifications share a maximum probability.

retrieval can be made. We assign a marine aerosol classification to areas classified as neither dust nor biomass burning aerosol.

[37] Figure 9 shows comparisons of monthly mean AOD in January and July 2006 which shows that background AOD is similar, independent of the aerosol classification used. In January we find AOD is generally 0.2–1 higher off the west coast of northern Africa when using the new aerosol classification, and in July a similar discrepancy is observed farther south. In these regions the GlobAerosol retrieval underestimates by 50–70% the total AOD observed using our speciation. Both of these regions correspond to areas of biomass burning outflow (Figure 5) suggesting that this is not captured well in the current GlobAerosol SEVIRI AOD. In July, evidence of dust transport across the Atlantic toward South America observed in the SDI data (Figure 5) is

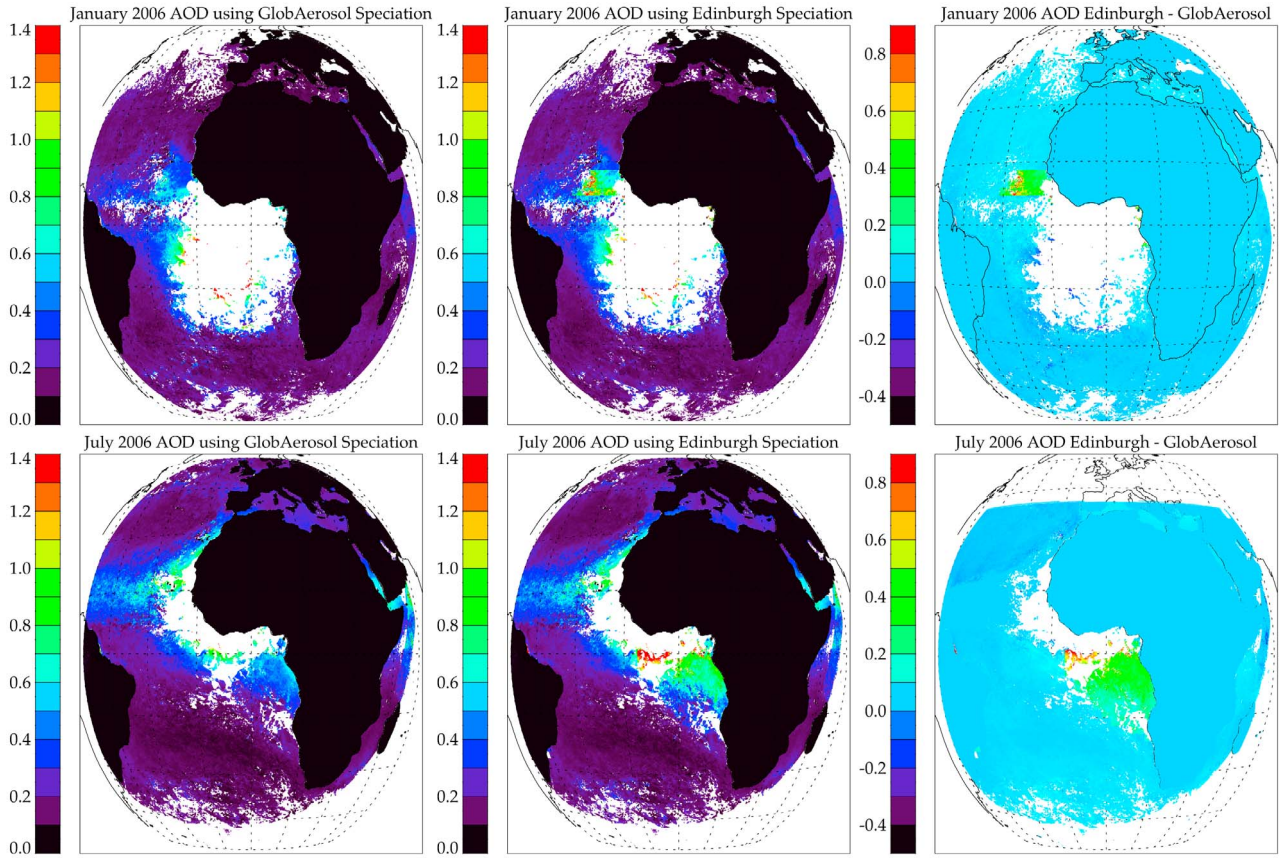

Figure 9. Monthly mean AOD in January and July 2006 retrieved from (left) speciation assigned using prior prescribed by the GlobAerosol algorithm assigned using retrieval cost and other quality control tests, (middle) speciation assigned using our aerosol distribution maps, and (right) the difference between the monthly mean. White areas denote persistent cloud or Sun glint where no retrieval is made. Continents where we are not examining the aerosol retrieval are colored black.

Table 1. Statistics Comparing the Satellite Angström Exponent Observations Using Lowest Cost Speciation (LC) and Our New Speciation (NEW) Against Level 2 AERONET Ground-Based Observations Between January 2004 and January 2008 Over Ascension Island and Cape Verde[a]

Location	Speciation	Correlation	RMS	Mean Difference (Retrieval - AERONET)	Mean Absolute Difference
Ascension Island	LC	0.26	0.46	0.07	0.37
Ascension Island	NEW	0.40	0.45	0.17	0.36
Cape Verde	LC	0.13	0.48	0.30	0.35
Cape Verde	NEW	−0.10	0.33	0.22	0.29

[a]Retrieved daily mean Angström Exponent is averaged over a 0.25 degree box centered on the AERONET location.

evident in both classifications and from this we determine that the ORAC dust and maritime aerosol models are similar enough to capture dust advection even if the wrong classification is made. This occurs because the refractive indices for the marine and dust OPAC aerosol models are similar.

[38] We also compare the satellite AOD and Angström Exponent over Ascension Island (7S, 14W) and Cape Verde (16°N, 22°W) with Aerosol RObotic NETwork (AERONET) data [*Holben et al.*, 1998] between January 2004 and January 2008. Table 1 shows comparative statistics between the satellite observations using our speciation, the lowest cost speciation and AERONET data. We exclude GlobAerosol retrievals where AOD is >2, indicative of cloud shadowing, and where the convergence cost is >10. To ensure no cloud contamination we only include days with more than 10 observations, and an AOD standard deviation below 0.2. The statistics are generated from daily mean values.

[39] Over Ascension Island we find that the Angström Exponent is more consistent with AERONET data when using our new speciation (r = 0.4 compared with r = 0.26). The AERONET Angström exponent is indicative of biomass burning aerosol during summer months which is rarely selected using the GlobAerosol "best type." We also find that our speciation increases the AOD correlation from 0.52 to 0.55 (not shown). Over Cape Verde there is poor correlation between the satellite observations and AERONET values using both speciations. In this case using our speciation does not improve the Angström Exponent correlation, but does improve the root mean square and mean difference statistics. Introducing our speciation prior has the greatest impact in regions of biomass burning aerosol where the aerosol properties are significantly different from those in other classes (e.g., dust and maritime aerosol). Over Cape Verde, improvements using our speciation are less marked as the OPAC descriptions of maritime and desert dust aerosol are similar. We acknowledge that comparing satellite and ground based observations is difficult given their different spatial scales. Significant work still remains to improve the correlation between satellite and ground-based observations of AOD reinforcing the statement that some caution must be exerted when using long-term satellite records of aerosol optical properties to determine aerosol forcing.

6. Summary and Concluding Remarks

[40] We used detailed observations from the DODO flight campaign in August 2006 to test the sensitivity of the ORAC dust retrieval to prior assumptions about aerosol size distribution, refractive index, and vertical distribution. We find that implementing the DODO size distribution and refractive index data into the retrieval at 0.55 μm with a fixed AOD of 0.5 increases simulated radiance by 10–20% with a larger bias observed at low solar zenith angles. We find that this discrepancy can be largely attributed to differences in the complex refractive index in the DODO and ORAC data, particularly within the FT. We test the sensitivity of the retrieval to the shape of the aerosol vertical distribution and find that given a fixed AOD this is unimportant in determining simulated radiance at 0.55 μm.

[41] We also provide time-dependent information to describe dust and biomass burning outflow from the African continent which we test in the ORAC retrieval during January and July 2006. We find similar background AOD but find discrepancies of 0.2–1 in AOD in regions of biomass burning outflow, where selecting the aerosol speciation based on the minimum cost function results in an underestimation of AOD by as much as 50–70% in the standard ORAC retrieval in comparison to our version. This indicates the importance of assumed aerosol composition for an accurate estimate of the AOD retrieval. Despite poorly identifying the "best type" in a given scene, GlobAerosol partially addresses this problem by providing optical depths for each of its assumed aerosol models, so that better approaches to identifying type can be applied post hoc. However, the extent to which such an approach can be successful is of course limited by the applicability of the assumed set of types. In particular, we find that biomass burning aerosol and dust often coexist in DJF meaning that none of the types in GlobAerosol may be appropriate, and AOD in such scenes with multiple aerosol layers cannot be correctly resolved.

[42] From the two pieces of complementary research presented above we conclude that satellite AOD retrievals are extremely sensitive to the properties assumed in the aerosol model, particularly the refractive index. We test a new method for classifying aerosol speciation, and suggest that our seasonal aerosol speciation could be included in a Bayesian retrieval which could use our probabilities, in conjunction with other information in the retrieval, to distinguish between aerosol classes with similar probabilities. This would improve the ability of the retrieval to capture continental aerosol outflow, which we have shown is particularly important for calculating AOD in regions of biomass burning.

[43] We acknowledge that this study is limited geographically and highlight the importance of field campaigns to accurately measure aerosol properties to inform satellite retrievals. Further research is necessary to quantify retrieval sensitivity to a priori for other aerosol types and retrievals, and this is of fundamental importance given the widespread use of satellite data by the scientific community to determine

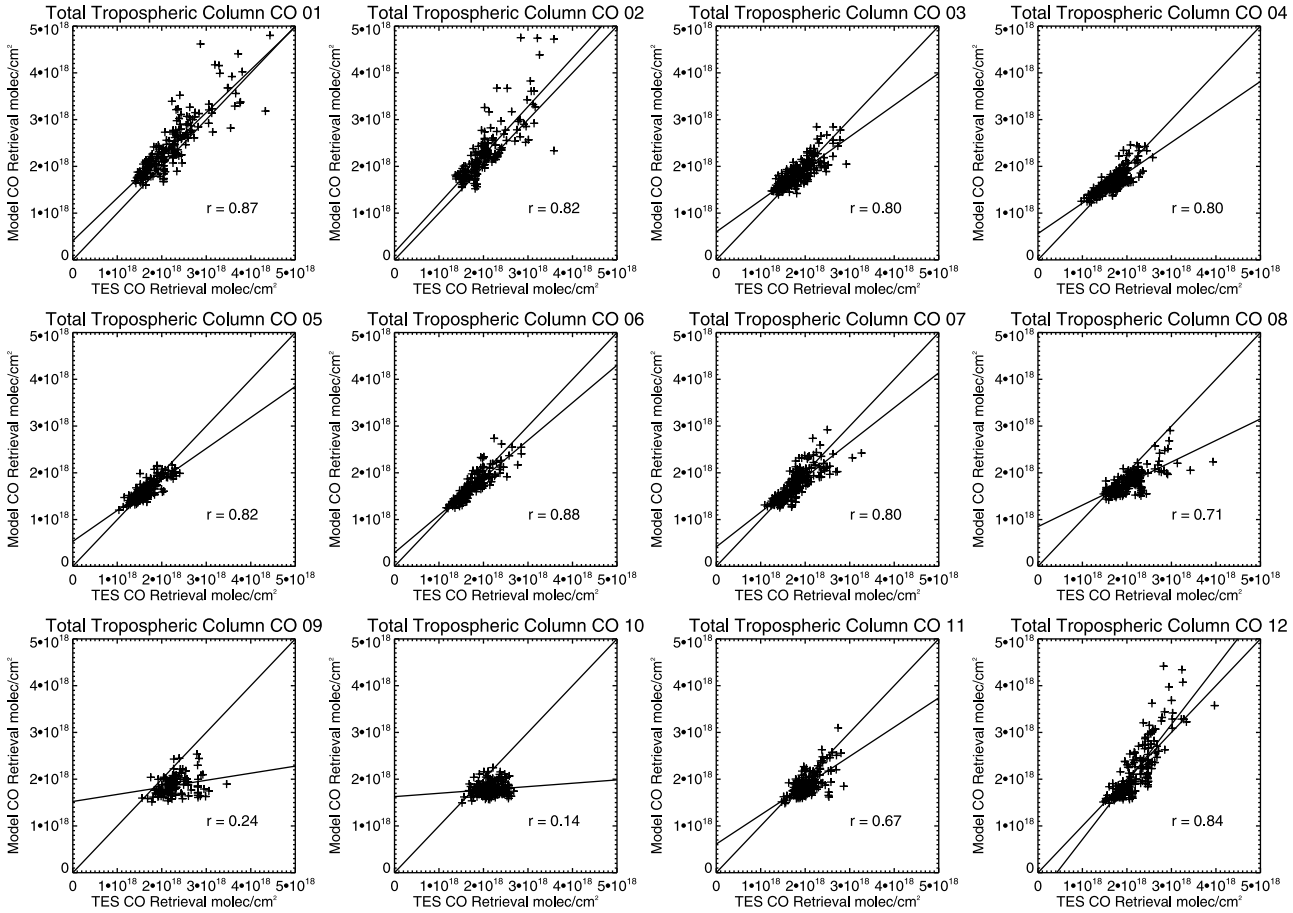

Figure A1. Monthly mean scatterplot of GEOS-Chem model and TES carbon monoxide column concentrations (molec cm^{-2}) during 2006 over the African continent (5°N–20°S, 10°E–35°W) compared on the model 2 × 2.5° grid. The correlation coefficient (r), the 1:1 line, and the line that best fits the data are shown inset into each panel.

aerosol forcing. Future missions with instruments capable of both AOD and trace gas retrievals, for example CO, could help to better constrain the a priori data used in AOD retrievals.

Appendix A: Description and Evaluation of GEOS-Chem Model CO Columns

[44] We use the GEOS-Chem CTM (v08.02.01), driven by assimilated GEOS-5 meteorology from the NASA Global Modelling and Assimilation Office (GMAO) at a 2 × 2.5° horizontal resolution. Our calculations use 47 vertical levels, extending from the Earth's surface to an altitude of 80 km, 29 of which are below 10 km, and assumed to be within the troposphere. Here, we describe only the details pertinent to the CO evaluation and refer the reader to more comprehensive model descriptions from P. Le Sager et al. (GEOS-Chem v8-02-01 online user's guide, 2008, http://acmg.seas.harvard.edu/geos/doc/man/). In this model, monthly CO and BC emissions from biomass burning are from the Global Fire Emission Database version 2 (GFEDv2) [*Collatz et al.*, 2007] and anthropogenic emissions of CO from the Emission Database for Global Atmospheric Research (EDGAR). We spin up the model for 6 months from July 2005 to January 2006, taking initial conditions from a full-chemistry run of the model.

[45] We use the Tropospheric Emission Spectrometer (TES) to evaluate GEOS-Chem CO columns from which we evaluate the spatial distribution of BC aerosol, as described in the main paper. The TES instrument, aboard the NASA Aura satellite, was launched in July 2004 in a near-polar Sun-synchronous orbit with an equator overpass time of 1345 LT, resulting in global coverage every 26 h. Here, we evaluate GEOS-Chem CO columns on the 2 × 2.5° model grid between 1200 and 1500 LT. To directly compare GEOS-Chem column CO with TES data we sample the model at the time and location of the TES retrieval and interpolate the GEOS-Chem profile onto the TES pressure grid (GEOS). We then apply a scene-dependent averaging kernel (**A**), which accounts for the vertical sensitivity of the TES instrument and the TES a priori (y_a) to give a model profile (y_{model}) as shown below:

$$y_{model} = y_a + \mathbf{A}(GEOS - y_a). \tag{A1}$$

[46] Figure A1 shows monthly comparisons of CO columns over the African continent, between TES observations and y_{model} measurements. Globally TES and GEOS-Chem

show good agreement with GEOS-Chem (not shown) capturing 45–81% of the variation in TES CO in all but JJA when the correlation coefficient (r) is <0.6, capturing <36% of the variability with a positive bias in GEOS-Chem CO. In order to check the representation of biomass burning emissions in our region of interest we reduce the comparison domain to focus on fire emissions from the African continent across the Atlantic (Figure A1), and find that the correlation increases between June and August (r = 0.71–0.88) but decreases significantly (r = 0.14–0.24) in September and October. In these months we find GEOS-Chem underestimates total column CO in this region but does show CO levels elevated above background values enabling us to use the model to describe the spatial distribution of biomass burning emissions. Underestimation of CO emissions in the GFED database seems the most likely cause of this discrepancy as the transport and chemistry in the model is sufficient to give high CO correlations in other months.

[47] **Acknowledgments.** C.E.B. is supported by NERC DARC studentship NER/S/D/2006/14345 and via additional support from the Rutherford Appleton Laboratory. DODO was funded by the NERC SOLAS grant NE/C517276/1. We thank the PIs Brent Holben and Didier Tanre for their efforts in establishing and maintaining the Ascension Island and Cape Verde AERONET sites.

References

Collatz, G. J., L. Giglio, P. S. Kasibhatla, J. T. Randerson, and G. R. Van der Werf (2007), Global Fire Emissions Database version 2, http://daac.ornl.gov/, Oak Ridge Natl. Lab., Oak Ridge, Tenn.

Diner, D., W. A. Abdou, H. R. Gordon, R. A. Kahn, Y. Knyazikhin, J. V. Martonchik, D. McDonald, S. McMuldroch, R. Myneni, and R. A. West (1999), Level 2 Ancillary Products and Datasets Algorithm Theoretical Basis, *JPL D-13402*, Jet Propul. Lab., Pasadena, Calif.

Diner, D. J., et al. (2008), Level 2 Aerosol Retrieval Algorithm Theoretical Basis, *JPL D-11400*, Jet Propul. Lab., Pasadena, Calif.

Dubovik, O., B. Holben, T. F. Eck, A. Smirnov, Y. J. Kaufman, M. D. King, D. Tanre, and I. Slutsker (2002), Variability of absorption and optical properties of key aerosol types observed in worldwide locations, *J. Atmos. Sci.*, *59*(3), 590–608.

Durant, A. J., S. P. Harrison, I. M. Watson, and Y. Balkanski (2009), Sensitivity of direct radiative forcing by mineral dust to particle characteristics, *Prog. Phys. Geogr.*, *33*(1), 80–102.

Engelstaedter, S. and R. Washington (2007), Atmospheric controls on the annual cycle of North African dust, *J. Geophys. Res.*, *112*, D03103, doi:10.1029/2006JD007195.

Foltz, G. R., and M. J. McPhaden (2008), Impact of Saharan dust on tropical North Atlantic SST, *J. Clim.*, *21*(19), 5048–5060.

Haywood, J., and O. Boucher (2000), Estimates of the direct and indirect radiative forcing due to tropospheric aerosols: A review, *Rev. Geophys.*, *38*(4), 513–543.

Hess, M., P. Koepke, and I. Schult (1998), Optical Properties of Aerosols and Clouds: The software package OPAC, *Bull. Am. Meteorol. Soc.*, *79*(5), 831–844.

Holben, B. N., et al. (1998), AERONET—A federated instrument network and data archive for aerosol characterization, *Remote Sens. Environ.*, *66*, 1–16.

Huang, J., C. Zhang, and J. M. Prospero (2009), Large-scale effect of aerosols on precipitation in the West African Monsoon region, *Q. J. R. Meteorol. Soc.*, *135*(164), 581–594.

Intergovernmental Panel on Climate Change (IPCC) (2007), *Intergovernmental Panel on Climate Change, Climate Change 2007: The Physical Science Basis, Summary for Policymakers. Working Group 1 Fourth Assessment Report*, Cambridge Univ. Press, Cambridge, U. K.

Johnson, B. T., S. R. Osborne, J. M. Haywood, and M. A. J. Harrison (2008), Aircraft measurements of biomass burning aerosol over West Africa during DABEX, *J. Geophys. Res.*, *113*, D00C06, doi:10.1029/2007JD009451.

Kokhanovsky, A. A., et al. (2010), The inter-comparison of major satellite aerosol retrieval algorithms using simulated intensity and polarization characteristics of reflected light, *Atmos. Meas. Tech.*, *3*, 909–932.

Liao, H., and J. H. Seinfeld (1998), Radiative forcing by mineral dust aerosols: sensitivity to key variables, *J. Geophys. Res.*, *103*(D24), 31,637–31,645.

Liu, D., Z. Wang, Z. Liu, D. Winker, and C. Trepte (2008), A height resolved global view of dust aerosols from the first year CALIPSO lidar measurements, *J. Geophys. Res.*, *113*, D16214, doi:10.1029/2007JD009776.

Liu, Z., et al. (2008), CALIPSO lidar observations of the optical properties of Saharan dust: A case study of long-range transport, *J. Geophys. Res.*, *113*, D07207, doi:10.1029/2007JD008878.

Marsh, S. H., S. M. Dean, R. G. Grainger, A. L. Quijano, G. E. Thomas, and B. N. Lawrence (2004), An optimal estimation aerosol retrieval scheme for ATSR-2, *Tech. Rep. Memo. 2004.2*, Atmos. Ocean. and Planet. Phys., Dep. of Phys., Univ. of Oxford, U. K.

Martonchick, J. V., D. J. Diner, K. A. Crean, and M. A. Bull (2002), Regional aerosol retrieval results from MISR, *IEEE Trans. Geosci. Remote Sens.*, *40*(7), 1520–1531.

McConnell, C. L., E. J. Highwwod, H. Coe, P. Formenti, B. Anderson, S. Osborne, S. Nava, K. Desboeufs, G. Chen, and M. A. J. Harrison (2008), Seasonal variations of the physical and optical characteristics of Saharan dust: Results from the Dust Outflow and Deposition to the Ocean (DODO) experiment, *J. Geophys. Res.*, *113*, D14S05, doi:10.1029/2007JD009606.

McConnell, C. L., P. Formenti, E. J. Highwood, and M. A. J. Harrison (2010), Using aircraft measurements to determine the refractive index of Saharan dust during the DODO experiments, *Atmos. Chem. Phys.*, *10*, 1–18.

Merchant, C. J. (2006), Saharan dust and SST bias: A dust index for daytime SEVIRI imagery, technical report, OSI-SAF Assoc./Visiting Sci. Project, Univ. of Edinburgh, Edinburgh, U. K.

Merchant, C. J., O. Embury, P. Le Borgne, and B. Bellec (2006), Saharan dust in nighttime thermal imagery: Detection and reduction of related biases in retrieved sea surface temperature, *Remote Sens. Environ.*, *104*, 15–30.

Mills, M., C. Ridame, M. Davey, J. La Roche, and R. J. Geider (2004), Iron and phosphorus co-limit nitrogen fixation in the eastern tropical North Atlantic, *Nature*, *429*, 292–294.

Osborne, S. R., B. T. Johnson, J. M. Haywood, A. J. Baran, M. A. J. Harrison, and C. L. McConnell (2007), Physical and optical properties of mineral dust aerosol during the Dust and Biomass-burning Experiment, *J. Geophys. Res.*, *113*, D00C03, doi:10.1029/2007JD009551.

Otto, S., E. Bierwirth, B. Weinzierl, K. Kandler, M. Esselborn, M. Tesche, A. Schladitz, M. Wendisch, and T. Trautmann (2009), Solar radiative effects of a Saharan dust plume observed during SAMUM assuming spheroidal model particles, *Tellus, Ser. B*, *61*, 270–296.

Rajot, J. L., et al. (2008), AMMA dust experiment: An overview of measurements performed during the dry season special observation period (SOP0) at the Banizoumbou (Niger) supersite, *J. Geophys. Res.*, *113*, D00C14, doi:10.1029/2008JD009906.

Remer, L. A., D. Tanré, and Y. Kaufman (2006), Algorithm for remote sensing of tropospheric aerosol from MODIS, *MOD04/MYD04*, NASA Goddard Space Flight Cent., Greenbelt, Md.

Rodgers, C. D. (2000), *Inverse Methods for Atmospheric Sounding: Theory and Practice*, World Sci., London.

Schmetz, J., P. Pili, S. Tjemkes, D. Just, J. Kerkmann, S. Rota, and A. Ratier (2002), An introduction to Meteosat Second Generation (MSG), *Bull. Am. Meteorol. Soc.*, *83*(7), 977–992.

Sinha, P., P. V. Hobbs, R. J. Yokelson, D. R. Blake, S. Gao, and T. W. Kirchstetter (2003), Distributions of trace gases and aerosols during the dry biomass burning season in southern Africa, *J. Geophys. Res.*, *108*(D17), 4536, doi:10.1029/2003JD003691.

Stammes, K., S.-C. Tsay, W. Wiscombe, and K. Jayaweer (1988), Numerically stable algorithm for discrete-ordinate-method radiative transfer in multiple scattering and emitting layed media, *Appl. Opt.*, *27*(12), 2502–2509.

Tegen, I., and I. Fung (1995), Contribution to the atmospheric mineral aerosol load from land surface modification, *J. Geophys. Res.*, *100*(D9), 18,707–18,726.

Thomas, G. E., S. M. Dean, E. Carboni, R. G. Grainger, C. A. Poulsen, R. Siddans, and B. J. Kerridge (2005), Globaerosol data user element: Aerosol extraction algorithm definition ATSR-2/AATSR algorithm theoretical basis document, *ATSR-2/AATSR*, Dep. of Atmos., Oceanic and Planet. Phys., Univ. of Oxford, Oxford, U. K.

Thomas, G. E., S. H. Marsh, S. M. Dean, E. Carboni, R. G. Grainger, C. A. Poulsen, R. Siddans, and B. J. Kerridge (2007), An optimal estimation aerosol retrieval scheme for (A)ATSR, *Tech. Rep. AOPP Memo. 2007.1*, Dep. of Atmos., Oceanic and Planet. Phys., Univ. of Oxford, Oxford, U. K.

Thomas, G. E., E. Carboni, A. M. Sayer, C. A. Poulsen, R. Siddans, and R. G. Grainger (2009a), *Oxford-RAL Aerosol and Cloud (ORAC): Aerosol Retrievals From Satellite Radiometers*, Springer, Berlin.

Thomas, G. E., C. A. Poulsen, A. M. Sayer, S. H. Marsh, S. M. Dean, E. Carboni, R. Siddans, R. G. Grainger, and B. N. Lawrence (2009b), The GRAPE aerosol retrieval algorithm, *Atmos. Meas. Tech.*, *2*, 679–701.

Wang, J., X. Liu, S. A. Christopher, J. S. Reid, E. Reid, and H. Maring (2003), The effects of non-sphericity on geostationary satellite retrievals of dust aerosols, *Geophys. Res. Lett.*, *30*(24), 2293, doi:10.1029/2003GL018697.

Watts, P. D., C. T. Mutlow, A. J. Baran, and A. M. Zavody (1998), Study on cloud properties derived from meteosat second generation observations, *Tech. Rep. 97/181*, EUMETSAT, Darmstadt, Germany.

Zhao, X. P., I. Laszio, O. Dubovik, B. N. Holben, J. Sapper, D. Tanré, and C. Pietras (2003), A study of the effect of non-spherical dust particles on the AVHRR aerosol optical thickness retrievals, *Geophys. Res. Lett.*, *30*(6), 1317, doi:10.1029/2002GL016379.

C. E. Bulgin, S. Gonzi, C. J. Merchant, and P. I. Palmer, School of GeoSciences, University of Edinburgh, Edinburgh EH9 3JN, UK. (cbulgin@staffmail.ed.ac.uk)

E. Carboni, R. G. Grainger, A. M. Sayer, and G. E. Thomas, Atmospheric, Oceanic and Planetary Physics, Clarendon Laboratory, Parks Road, Oxford OX1 3PU, UK.

E. Highwood, Department of Meteorology, University of Reading, Reading, RG6 6BB, UK.

C. A. Poulsen and R. Siddans, Rutherford Appleton Laboratory, Didcot OX11 0QX, UK.

C. L. Ryder, Department of Physics, Imperial College, London SW7 2AZ, UK.